

An X-ray Investigation of Three Supernova Remnants in the Large Magellanic Cloud

M. D. Klimek¹, S. D. Points, R. C. Smith

Cerro Tololo Inter-American Observatory, National Optical Astronomy Observatory, Casilla 603, La Serena, Chile

spoints@ctio.noao.edu, csmith@ctio.noao.edu

R. L. Shelton

Department of Physics and Astronomy, University of Georgia, Athens, GA 30602

rls@physast.uga.edu

and

R. Williams

Columbus State University, Coca-Cola Space Science Center, 701 Front Ave., Columbus, GA, 31901

rosanina@ccssc.org

ABSTRACT

We have investigated three SNRs in the LMC using multi-wavelength data. These SNRs are generally fainter than the known sample (see §4) and may represent a previously missed population. One of our SNRs is the second LMC remnant analyzed which is larger than any Galactic remnant for which a definite size has been established. The analysis of such a large remnant contributes to the understanding of the population of highly evolved SNRs.

We have obtained X-ray images and spectra of three of these recently identified SNRs using the *XMM-Newton* observatory. These data, in conjunction with pre-existing optical emission-line images and spectra, were used to determine the physical conditions of the optical- and X-ray-emitting gas in the SNRs. We have compared the morphologies of the SNRs in the different wavebands. The physical properties of the warm ionized shell were determined from the H α surface brightness and the SNR expansion velocity. The X-ray spectra were fit with a thermal plasma model and the physical conditions of the hot gas were derived from the model fits. Finally, we have compared our observations with simulations of SNR evolution.

Subject headings: supernova remnants — X-rays: diffuse background

1. Introduction

Supernovae (SNe) and their remnants are the driving force behind the dynamic interstellar medium (ISM) of our Galaxy and others. The study of the energetics and evolution of supernova remnants (SNRs) thus forms the foundation

for developing a complete understanding of the complex structure and evolution of the ISM in gas-rich galaxies not unduly affected by external events such as galaxy-galaxy collisions. However, in order to form an accurate picture of how SNRs influence the ISM, it is necessary to have a complete and unbiased sample of SNRs in a galaxy. This is very difficult within the Milky Way as dust absorption and confusion along the line-of-sight

¹Present email address: klimek@physics.utexas.edu

hinders our ability to detect and determine the physical conditions of Galactic SNRs. Although it is possible to obtain a more complete sample of SNRs in more distant galaxies, their distance hinders the investigation of their physical conditions in detail.

The Large Magellanic Cloud (LMC) offers the ideal laboratory for the study of a large sample of SNRs. The LMC is well out of the Galactic plane and thus offers low foreground absorption ($A_V \sim 0.3$). Meanwhile, its distance is relatively well known (~ 50 kpc; Di Benedetto (2008), Feast (1999)) and distances within the LMC are small compared with its distance to us so all objects within the LMC can be taken to be at approximately the same distance. Its proximity also allows us to resolve a great amount of spatial detail ($1'' \approx 0.25$ pc).

The SNRs presented in this paper were discovered as regions of shock-ionized gas in the Magellanic Cloud Emission Line Survey (MCELS) using the reliable [S II]/H α diagnostic (Fesen et al. 1985), with SNRs typically having [S II]/H α > 0.4 (Levenson et al. 1995). Analysis of archival *ROSAT* data and high resolution optical spectra confirmed these shells as SNRs (Smith et al. (2011, in preparation), Smith et al. (2003)). However, the *ROSAT* observations are too shallow to provide much detailed information on the hot gas within these remnants. Two of these remnants have been detected, but not classified as SNRs in the *ROSAT* survey of the LMC (Haberl & Pietsch 1999), and the Parkes radio survey (Filipovic et al. 1998). Blair et al. (2006) searched for FUV emission from these remnants but failed to detect them.

A thorough investigation of the hot gas is crucial to understanding the properties of the SNR and its interaction with the host galaxy. SNRs contribute most of the hot gas component of the ISM, and much of the energy originally released in the supernova event is carried as thermal energy in the hot gas. Moreover, the interaction between the hot interior and the cool shell of shocked material dictates the evolution of the SNR. We have therefore obtained new X-ray data from the *XMM-Newton* observatory and analyzed these data along with the optical data from MCELS to form a complete picture of these SNRs.

Our observations and analysis techniques are

presented in §2. In §3 we give the results of these techniques applied to the individual objects, followed by discussion of those results in §4. A brief conclusion is given in §5.

2. Observations

2.1. X-ray

XMM-Newton is an orbiting X-ray observatory operated by the European Space Agency. In this study, we use data from the European Photon Imaging Camera (EPIC) MOS CCDs. These are two identical devices each mounted behind 58 nested Wolter type 1 mirrors. The EPIC cameras offer the capability to perform extremely sensitive imaging observations over the telescope’s field of view of 30 arcmin and in the energy range from 0.15 to 15 keV with moderate spectral ($E/\Delta E \sim 20-50$) and angular resolution (point-spread function: 6 arcsec FWHM). For further technical discussion, see Turner et al. (2001).

This study presents new X-ray data from *XMM-Newton* on three LMC SNR candidates: SNR0449–6921, SNR0506–6542, and SNR0537–6628. Proposed pointings were chosen to follow up on regions of high [S II]/H α from the MCELS data. Three observations are presented in this paper. See Table 1 for details on the observations.

These data were processed with the Extended Source Analysis Software (ESAS) package. ESAS is a package of perl scripts which call commands from ESA’s Science Analysis Software and standalone FORTRAN 77 programs following analysis techniques given by Snowden et al. (2008). ESAS automatically filters times of high background contamination and poor event grades.

The low X-ray surface brightness of these SNRs, in combination with limits of X-ray coverage and resolution from past surveys, explains their non-detection until the present. We will show that the average X-ray surface brightness of these remnants falls below the lowest levels detected from LMC SNRs included in earlier catalogs. Given the relatively small number of source counts we are able to collect from the remnants, we need to have a good understanding of the backgrounds so that we can accurately extract source properties from limited data.

After the data had been filtered, we applied the

ESAS `cheese` task, which uses SAS tools to identify point sources, and creates a mask file. We specifically ran the source detection over a band from 0.8 to 8.0 keV in order to identify troublesome nonthermal background sources without falsely masking softer lumpy features within the SNR emission.

Using these masks, we then extracted spectra from background regions near the remnants. We binned these background spectra to 50 counts per channel and fit them with NASA’s Xspec package using a model composed of two gaussian components to account for the strong Al and Si $K\alpha$ fluorescent lines near 1.5 and 1.75 keV, respectively, an APEC component for the Local Hot Bubble/Solar Wind Charge Exchange, an absorbed APEC component for the Milky Way’s halo, and an absorbed power law component for the non-thermal extragalactic background. The photon index of the extragalactic power law was fixed at 1.46 (Snowden et al. 2008; Chen et al. 1997). Finally, we also included a power law component which was not folded with the instrumental response to model residual soft proton contamination not removed in the light curve filtering. The specifics of the background modeling are discussed below for each observation, but aside from the soft proton contamination which varies with time, the background parameters found by this method are consistent between all the observations. In addition, our temperature for the local hot bubble in SNR0449–6921 and SNR0537–6628 are consistent with the results of Henley & Shelton (2008). An example of our background model is seen in Figure 1.

Next we extracted spectra of the SNR emission and fit each with the corresponding background model, plus an APEC thermal plasma component, with abundances set to the canonical LMC value of 0.3 solar. We froze the temperatures, photon indices, column density, and gaussian parameters as determined from the background fit, but allowed the normalizations to vary to account for the change in area between the background and source spectrum extraction regions. The source spectra generally have few energy bins with significant numbers of counts, but the constraints provided by the background fits allowed us to achieve statistically significant fits for the source parameters. Fits using the older Raymond-Smith model

or the MEKAL model in place of the APEC model gave nearly identical results. After this initial fitting, we added the additional constraint that the ratio of the normalizations of the absorbed thermal and nonthermal components should remain constant over the field-of-view. This constraint did not change the best-fit values that we found, but did improve the uncertainties in the fitted values. An example of the residuals from our background model fitted with the APEC model is seen in Figure 2.

We compared our fitted values of hydrogen column density with that found in HI surveys. We used the Leiden/Argentine/Bonn survey of Galactic hydrogen (Kalberla et al. 2005) and the ATCA+Parkes survey of LMC hydrogen (Kim et al. 2003). It has been shown (Arabadjis & Bregman 1999) that above $N_{\text{H}} > 5 \times 10^{20} \text{ cm}^{-2}$, the total X-ray absorption column increases by about a factor of 2 over the HI-derived value due to molecular hydrogen. We must also remember that only part of the LMC column is actually in front of our objects. Thus we should expect our fitted values to be close to $2N_{\text{H}}^{\text{Gal}} + N_{\text{H}}^{\text{LMC}}$, where N_{H}^{X} is the value quoted from the respective survey. In every case, we found that our fitted values of N_{H} are consistent with the survey values.

Finally, we compared the observed X-ray spectrum with simulations. We simulated each SNR with the aid of a computer code that followed the hydrodynamics of the plasma on a spherically-symmetric Lagrangian mesh, simulated the shock front, shock heating, thermal conduction of heat from the remnant’s hot center outwards, radiative cooling by non-collisional ionizational equilibrium (non-CIE) plasma, and, when needed, nonthermal pressure due to magnetic fields and cosmic rays. The products of our simulations, the temperature, density, and ionization level as a function of location within the SNR and SNR age, were used to calculate the spectra in a non-CIE manner. The algorithms are described in detail in Shelton (1998). The spectra were then converted to Xspec models with age as a free parameter. To accomplish the spectral fitting in Xspec, we used the fit to the source region as described above, and assumed the APEC source component accurately models the SNR plasma emission. We then deleted the APEC component and replaced it with

the simulated spectrum. We stepped through the spectra at various ages and searched for a minimum in the Chi-squared. The simulations were run assuming solar abundances. As a first approximation, we varied the normalization of the resulting spectral model to account for the different abundances of the LMC.

We also used ESAS to produce combined and adaptively smoothed images in three bands (0.35-0.85, 0.85-2.0, and 2.0-8.0 keV) with a kernel of 15 counts. The ESAS task `proton` uses the soft proton contamination model parameters found in the background fitting to subtract this component from the images.

Given the thermal plasma model normalization A we can calculate the electron density in the hot gas by $n_e = 3.89 \times 10^7 D \sqrt{A/V_{\text{hot}}}$ where D is the distance to the SNR, A is the normalization of the plasma model component, and V_{hot} is the volume of the hot gas in cgs units. The mass of the hot gas is $M_{\text{hot}} = 1.17 n_e m_p V_{\text{hot}}$, assuming fully ionized helium and where m_p is the proton mass. Given the temperature from our spectral fits, the total thermal energy is then $E = (3/2) N k T = 4.60 \times 10^{-9} n_e V_{\text{hot}} T$, where T is the temperature of the plasma model in keV. We can also find the pressure as $P_{\text{hot}} = n k T = 3.05 \times 10^{-9} n_e T$. These calculated values are listed in Table 2. The errors are the one sigma uncertainties estimated by Xspec in the fit process propagated through the above equations.

2.2. Optical

Optical images came from the MCELS project (Smith et al. 2000) where these remnants were originally identified. The observations consist of red and green continuum images and H α , [S II], and [O III] emission line images from the Curtis Schmidt Telescope at the Cerro Tololo Inter-American Observatory (CTIO). The final images are flux calibrated and rescaled to have 2" pixels. The continuum exposures were used to subtract the continuum contribution to the emission line images.

In addition, we have long-slit, high-dispersion echelle spectra of the SNR candidates from the CTIO 4m telescope. The data have a 24 μ m pixel size that corresponds to 0.082 Å (3.65 km s⁻¹) along the dispersion axis and $\sim 0''.26$ along the

sky. The spatial coverage along the slit is roughly 3', limited by the optics of the camera. Details of the reduction of these data can be found in Smith et al. (2011, in preparation).

The echelle profile of the H α line is broadened along the dispersion axis both by the inherent instrumental profile (~ 14 km s⁻¹) and by thermal Doppler broadening (~ 18 km s⁻¹ at X-ray temperatures). To assign an expansion velocity to each remnant, we extract profiles along the dispersion axis where the emission shows the greatest dispersion and measure the peaks of the profile.

Using the flux-calibrated MCELS images, we measured an H α surface brightness and the average radius R and thickness ΔR of the shell. For a uniform spherical shell, the greatest line of sight through the shell is $\mathcal{L} = 2\sqrt{R^2 - (R - \Delta R)^2}$. The measured surface brightness then implies an emission measure $\text{EM} \equiv n_e^2 \mathcal{L} = 5 \times 10^{17} \times \text{SB}$ where SB is the surface brightness in cgs units and arcseconds. The total mass of the warm ionized shell is $M = 1.27 n_e m_p V_{\text{shell}}$, where V_{shell} is the volume of the shell and assuming singly ionized helium. Expansion velocities v_{exp} have been determined from echelle spectra of the H α emission-line, and thus we may determine kinetic energies for the warm shells by $K = M v_{\text{exp}}^2 / 2$. If we assume that $T = 10^4$ K, we can also calculate the pressure in the shell as $P_{\text{shell}} = 2 n_e k T = 2.76 \times 10^{-12} n_e$.

In calculating the volume of the shell, we assumed an ellipsoidal geometry, measuring two axes from the projected face of the shell and taking the third line-of-sight axis to be the average of these two. We then took the uncertainty in the radius along this third axis to be the deviation of the first two axes from their mean. We also considered the instrumental and Doppler broadening of our echelle spectra as an additional source of error. Convoluting the two profiles, we found an uncertainty of 11 km s⁻¹. Calculated quantities are listed in Table 2.

The age of the SNR may be estimated using the analytic expressions of the Sedov-Taylor solution for blast wave expansion, in which the shell radius is given as a function of time by $r(t) = 1.17 (E t^2 / \rho)^{1/5}$, where E is the explosion energy and ρ is the ambient density. Taking the time derivative and applying the Rankine-Hugoniot conditions for a strong shock to relate the blast wave velocity to the post-shock gas ve-

locity u , we find $u(t) = 0.351(E/\rho t^3)^{1/5}$. Solving this system yields $t = 0.3(r/u)$. We then obtain the ages by plugging in the radius observed in the optical images and the velocities from the echelle spectra. These procedures apply best to remnants that are still in the Sedov-Taylor phase of evolution, since post-Sedov-phase remnants continue to expand at a slower rate. The Sedov-Taylor phase is expected to end when the post-shock gas velocity drops to $\sim 190 \text{ km s}^{-1}$. Inhomogeneities in the ambient medium also affect the expansion rate. In addition, the observed velocities and radii are found for individual parts of the SNRs and, due to asymmetries in the SNRs may not adequately represent the whole objects. All of these effects combine to make the ages estimated from $t = 0.3(r/u)$ approximate.

The simulations described previously also provide an independent numerical estimate of the age. Alternatively, given the present values of r and u , one may solve for the ratio E/ρ , or equivalently E/n where n is the ambient number density, and compare this with the value estimated using the X-ray spectral modeling and $\text{H}\alpha$ surface brightness techniques as described above.

3. Results

3.1. SNR0449–6921

SNR0449–6921 shows the simplest structure of the three remnants presented here. Its well defined [S II] shell surrounds a smooth elliptical distribution of soft X-ray emission with radii of $1.3' \times 0.75'$ or $19.4 \times 11.25 \text{ pc}$. The shell has typical values for [S II]/ $\text{H}\alpha$ of ~ 0.6 , as opposed to maximum values ~ 0.2 elsewhere. The bright $\text{H}\alpha$ emission to the east of SNR0449–6921 comes from the H II region N79 and is not directly related to our study. See Figures 3 and 4.

N79 corresponds to an area of diffuse soft X-ray emission which covers half the XMM field of view. We defined a circular source region covering the SNR and then divided the field of view into two background regions corresponding to the area covered by the diffuse X-ray emission and the empty area. The spectra from the two background regions were fit simultaneously with independent normalizations but other model parameters tied together. In the region with diffuse X-rays we included an additional absorbed thermal compo-

nent.

SNR0449–6921 shows a clear bow-shaped expansion pattern in the echelle spectrum. It is difficult to discern a complete corresponding blueshifted pattern. It may be obscured by the broad band of emission from the surrounding H II region if SNR0449–6921 is moving away along our line of sight with respect to the systemic velocity. Some blueshifted emission is seen along the right side of the spectrum. Taking this to be the front edge of the shell, we measured a velocity of $\pm 70 \text{ km s}^{-1}$.

We found a best-fit temperature for the local hot bubble of $kT = 0.11 \text{ keV}$, and for the Galactic halo of $kT = 0.27 \text{ keV}$. In the region with the diffuse soft X-rays we found an additional absorbed thermal component with $kT = 0.19 \text{ keV}$. Best-fit hydrogen column density is $3.7 \times 10^{21} \text{ cm}^{-2}$. Full details of the background fit are found in Table 3.

Unfortunately all but 7 ks of this observation was lost to flaring events. This combined with the fact that SNR0449–6921 is small and faint resulted in too few source counts to constrain the SNR properties, even with the information provided by the background fits. However, by defining emission above 1.5 keV as hard, we can estimate a hardness ratio of -0.97. Based on the clear detection of soft X-ray emission confined within a well-defined shell of enhanced [S II]/ $\text{H}\alpha$ optical emission, we identify this candidate as a bona fide SNR.

3.2. SNR0506–6542

SNR0506–6542 (DEM L 72, FHW95 B0505-6548) shows a clear shell structure in the optical data with [S II]/ $\text{H}\alpha$ between 0.5 and 0.7. It is isolated from any other diffuse optical or X-ray emission. It is roughly circular along the north edge, but flattened along the eastern side. The southwestern edge shows a bright flat region with complex filamentary structure. There appears to be a gap in the shell along the southern edge but closer investigation shows faint optical filaments extending southwestward and reconnecting with the flat region mentioned above. Complex filamentary structure is visible inside the shell. We also see a filament extending northeast from the remnant. The fainter filaments are most clearly visible in [O III] images. The optical shell

and X-ray emission cover $7.3'$ or 110 pc along a northwest-southeast line, and $6.7'$ or 100 pc along a northeast-southwest line. A northeastern spur extends a projected distance of $1.2'$ or 18 pc east of the main shell. For the purposes of our calculations, we assign a definite size to the remnant by fitting an ellipse with radii of $2.7'$ and $4.0'$, or 40 pc and 60 pc, to the shell. This ellipse encompasses the main body of the shell, along with the northeastern spur and the faint filament bounding the southern edge. The shell is filled with diffuse soft X-ray emission but it is not as evenly distributed as in SNR0449–6921. Several local maxima are observed. The X-ray emission seems to divide itself into three regions, one in the northwest corner, a second within the southern bulge, and a third along the eastern side, fully contained by the northeastern spur. The emission from this last region seems to be generally fainter than that from the other two regions. See Figures 5 and 6.

We detected emission across the face of SNR0506–6542 in the echelle spectra, although the pattern is not smooth. Rather it shows several areas of convergence toward or deviation from systemic velocity. The systemic component is distinguished from the telluric OH line. Maximum inferred shell velocities are $\pm 90 \text{ km s}^{-1}$.

In the XMM data, we defined a circular source region covering the SNR and extracted the remainder of the FOV as the background. After light curve filtering we were left with 9 ks of integration time. We found a best fit temperature for the local hot bubble as $kT = 0.09 \text{ keV}$ and for the Galactic halo as $kT = 0.2 \text{ keV}$, consistent with the results from the SNR0449–6921 background. The best fit column density is $3.2 \times 10^{21} \text{ cm}^{-2}$. Using these background parameters, we fit our source region with an additional thermal plasma and found a gas temperature of $kT = 0.17 \text{ keV}$.

3.3. SNR0537–6628

SNR0537–6628 (DEM L 256) also lies projected near the H II regions DEM L 251, 253, and 264. Optical filaments take the form of two nested shells. The inner shell is complete and has a radius of $0.8'$ or 11.6 pc. The outer shell covers roughly 180° on the southeast half of the remnant with a radius of $1.6'$ or 23 pc along its western extent and $1.3'$ or 20 pc in the perpendicular direction. Two clumps of H α emission appear on the west-

ern side of the remnant. One clump lies along the inner shell, and the second is roughly co-circular with the outer shell. Our [S II]/H α ratio maps reveal that these clumps have ratios of < 0.4 , similar to the nearby H II regions and in contrast to the values > 0.7 found in the shell filaments. Thus it seems that these clumps are not actually associated with the SNR. The X-ray emission is confined to the eastern half of the remnant corresponding to the extent of the outer H α shell and appears to be contained primarily between the two filaments. See Figures 7 and 8.

This SNR shows clear blue- and redshifted expansion patterns across the face, although the redshifted emission is considerably stronger than the blueshift counterpart. A wide band of H α emission is also visible from the surrounding H II region. The expansion pattern has two distinct sections, with distinct central velocities but equal expansion velocities of $\pm 55 \text{ km s}^{-1}$. The break between the two patterns corresponds to the point where the echelle slit crosses the inner optical shell. Strong H α emission is seen converging to the systemic velocity at the location of the outer half-shell. A corresponding convergence on the other end of the slit is much fainter, but this end of the slit does not intersect any part of the outer half-shell.

There is diffuse soft X-ray emission around the edge of the XMM field of view in the direction of DEM L 256. In this exposure, 20 ks of integration time were useable. We extracted a background annulus around the SNR that is small enough to avoid the emission associated with the H II regions. Here we found best-fit temperatures of $kT = 0.17 \text{ keV}$ for the local hot bubble and $kT = 0.22 \text{ keV}$ for the Galactic halo, again consistent with the above findings. Column density is fit as $5 \times 10^{21} \text{ cm}^{-2}$. Fitting the center of the annulus with this background plus a source plasma gave a gas temperature of $kT = 0.22 \text{ keV}$.

4. Discussion

The [S II]/H α ratio technique has been used before to discover SNRs which were too faint to be detected in previous surveys, for example, Williams et al. (2004) and Stupar et al. (2007). This technique when applied to the detailed and deep MCELS images turned up yet more SNR candidates which had been missed in previous optical

studies¹. Using the thermal source models fitted to the X-ray spectra, we can derive a flux which can be converted to an estimated *ROSAT* High Resolution Imager count rate using the PIMMS tool from HEASARC. We found that *ROSAT* would have collected roughly 1.3×10^{-4} counts per second per square arcminute from SNR0506–6542 and 3×10^{-4} from SNR0537–6628 over its primary energy band of 0.2–2.0 keV. We were not able to calculate a flux for SNR0449–6921 since its spectrum was of too poor quality to achieve a satisfactory fit. However we can set an upper limit on its flux by assuming that all emission from the source region is due to a single absorbed thermal plasma. In this way we found a flux of 5.0×10^{-14} erg s⁻¹ cm⁻² corresponding to 2.1×10^{-3} counts per second per square arcminute for *ROSAT*. We found that the two remnants presented here for which we have good flux measurements are indeed fainter than all *ROSAT* detected LMC remnants from the catalog of Williams et al. (1999). Our upper limit for SNR0449–6921 is higher than three of the *ROSAT* SNRs, but among those, one benefitted from a lengthy 109 ks exposure, and the other two detections are of too poor quality to allow a discussion in that reference. We also note that SNR0537–6628 coincides with HP 344, although that object was not identified as a SNR candidate (Haberl & Pietsch 1999). Again using PIMMS to convert our measured flux to a *ROSAT* PSPC count rate over the range 0.1–2.4 keV we found an expected rate of 1.6×10^{-2} counts per second, which compares favorably with the rate of $(1.4 \pm 0.2) \times 10^{-2}$ counts per second from Haberl & Pietsch (1999).

Our technique can not be expected to identify the complete population of faint SNRs, however. As discussed in Chu (1997) and Chu & Mac Low (1990), SNRs in superbubbles cleared out by OB associations lack the optical shell signature. Several SNRs have been discovered within LMC superbubbles (SBs) solely by their X-ray emission in *ROSAT* mosaics. Based on the success of the present project in identifying previously unknown faint remnants, it seems likely that more such remnants exist, but may be lacking in optical signatures. A deep X-ray survey of SBs with modern

instruments would be necessary to fill out the population of LMC remnants. Since the spectra of SNRs soften as they age, instrumentation with enhanced sensitivity to low energy photons would be especially beneficial.

Superbubbles in the LMC are often in excess of 100 pc, so the comparatively small sizes of these objects, as well as the lack of interior OB associations, argues for their formations as single SNRs, rather than as SBs. Likewise, SBs tend to have fairly slow expansion velocities, close to those of the surrounding ISM. The derived expansion velocities are on the low side for SNRs, but are higher than one would expect for a SB (Dunne et al. 2001). Only SNR0506–6542 is of comparable size to these SBs but has a higher expansion velocity, which argues for an SNR origin. SNR0449–6921 and SNR0537–6628 are on the high side of velocity for SBs, are notably smaller than typical SBs, and do not have any known OB associations, which suggests that they also are likely SNRs.

We can estimate the density of the ambient ISM by summing the masses of the warm shell and hot gas and dividing by the volume of the remnant. Technically one should also subtract the mass of the progenitor star, but in all three cases here the SNR masses are now much greater than a typical progenitor mass of $\sim 10M_{\odot}$. Moreover, this ISM density estimate will be strongly affected by the same approximations mentioned in §2 with respect to calculating the shell mass, so these are at best a rough estimate. For SNR0449–6921, we were unable to fit a model to the source plasma and so we do not have information on the density of the hot gas. In this case, we included only the mass of the shell and calculated a lower limit of ~ 4 cm⁻³ on the ambient density. Even this lower limit is significantly higher than the densities of 0.6 and 1.4 cm⁻³ which we estimated for SNR0506–6542 and SNR0537–6628 respectively. This is consistent with the observation that SNR0449–6921 seems to be embedded in an H II region.

An additional motivation for studying SNR0449–6921 was its close projection to the ring nebula around the Wolf-Rayet star Br2. This ring nebula is unusual in its bright nebular He II $\lambda 4686$ line emission, indicating very high excitation (Garnett & Chu 1994). Two other examples of He II-emitting nebulae are known in the LMC: the He II nebula around the X-ray binary LMC

¹See for example Williams et al. 2010 (in preparation) and references therein, online at <http://hoth.ccsc.org/mcsnr/>

X-1 (Pakull & Angibault 1986) and N44C which has been suggested to be ionized by the transient LMC X-5 (Pakull & Motch 1989). Later studies demonstrated that the He II and H α line widths in the ring nebula are too narrow to be caused by dynamical interaction with the expanding SNR shell (Chu et al. 1999). However, the possibility of excitation by an X-ray source within the ring (e.g., Chu et al. 2000) or within the SNR had not been ruled out. Our observations found no significant compact X-ray emission at the location or Br2. Furthermore, we see a smooth distribution of soft emission within the SNR shell with no indications of any compact or hard source.

The very irregular shell morphology of SNR0506-6542 makes it difficult to assign it an exact size. Measured at the extreme extents of the optical shell, it has radii of 50×55 pc which would make SNR0506-6542 the largest known SNR in the LMC, larger even than SNR 0450-70.9 (Williams et al. 2004). However, for the purposes of our quantitative estimates, we take a shell size of 40×60 pc, as mentioned above. The brightest X-ray emission is seen in the western half of the SNR. Here the optical shell flattens and becomes thicker and more filamentary. Many optical clumps are also seen in this half of the shell. This is consistent with the SNR encountering a region of higher ISM density which is being shocked by the blast wave. As this material passes through the shock, it evaporates producing diffuse X-ray emission. The faint optical filament along the extreme eastern edge of the remnant coincides with a line of X-ray emission. This shock front may still be capable of heating the gas it encounters to X-ray emitting temperatures. Elsewhere along the northern rim we see less emission along the shell and, in some areas, a gap between the optical shell and interior X-ray emission, suggesting that the shock front here is no longer powerful enough to fully ionize new gas and that previously heated gas has now cooled to below detectable levels.

The expansion velocity of 90 km s^{-1} implies an age of ~ 150 kyr. Solving for E/n as described in §2 gives $E/n = 2.6 \times 10^{51} \text{ erg cm}^3$, in excellent agreement with the values calculated from the H α surface brightness and X-ray spectrum as listed in Table 2. However, such slow-moving shocks would not be capable of heating new gas to X-ray emitting temperatures. Post-shock velocities of ~ 140

km s^{-1} are needed to heat gas to a sufficient temperature to radiate strongly at 0.2 keV. The evidence for newly shock-heated gas seen in the X-ray images may indicate that for at least some portions of the SNR front, the velocity is well in excess of 90 km s^{-1} . If we instead consider the expansion velocity to be 140 km s^{-1} , we find an age of 95 kyr. This is an issue seen in other remnants, e.g. N86 and N11L. It may be that the optical material with the greatest Doppler shifts has too low surface brightness for detection in echelle spectra. In any case, the observed gas velocities are well below those expected at the end of the Sedov-Taylor phase, and thus the age of 150 kyr is likely an overestimate. For comparison, an SNR of this radius but with gas velocity corresponding to the end of the Sedov-Taylor phase would give an age of ~ 80 kyr.

When applying the simulated spectrum, we found a best fit at an age of 80 kyr. However, the simulations seem to underpredict the prominent emission lines around 0.6 keV. This could indicate that we have underestimated the abundances throughout our fitting process. Returning to the background model and allowing the local hot bubble abundance to float, we found a best fit when $Z_{\text{LHB}} = 1.9$. Applying the background model to the source spectrum we again found a best fit to the SNR emission when the source plasma abundances are set to 0.5. Plugging in the simulated spectrum we found that an age of 100 kyr is now preferred, in better agreement with the analytically derived values. However, one might expect that such an old remnant would be heavily dominated by the swept-up medium, and therefore show abundances close to those of the LMC. Furthermore, such an old remnant will have evolved past the Sedov-Taylor phase which ends at velocities

It is worth pointing out that the physical parameters which we derived for this SNR are broadly similar to those found by Williams et al. (2004) for SNR 0450-70.9. Prior to that study, no interior X-ray emission had ever been detected from a remnant of this size. Moreover, no remnant of this size is known within our galaxy. Thus, a detailed study of two such advanced SNRs represents a significant step forward in our understanding of the long-term fate of these objects. We also note that P_{hot} is significantly greater than P_{shell}

for this remnant, suggesting some pressure-driven expansion even at these late ages.

X-ray emission from SNR0537–6628 appears to trace the H α filaments, again suggesting that this gas is recently shock heated. The appearance of two distinct shells along with two expansion patterns in the echelle spectrum which correlate with the optical shells suggests a bilobed structure for the SNR. The near edge of the SNR seems to be encountering denser material as evidenced by the X-ray emission corresponding to that shock wave and the stronger H α emission converging to systemic velocity on that edge.

The observed expansion velocity of 55 km s⁻¹ is quite low and gives an age of 125 kyr. The corresponding ratio $E/n = 6 \times 10^{49}$ erg cm³ does not agree as well with the observed value of 1.6×10^{50} erg cm³. However, the thermal energy of the hot gas was estimated assuming filling of an entire ellipsoidal shell, whereas we see X-ray emission from only the eastern half. Furthermore, if this is a bilobed structure which is not aligned with the line of sight, we are only measuring a projected component of the true expansion velocity. Both of these considerations would bring the two numbers into closer agreement. We calculate that the viewing angle of the bilobed expansion would need to be $\sim 40^\circ$ in order for the two numbers to agree. We also note that if the observed elliptical region of X-ray emission were actually a circular disc, a viewing angle of $\sim 55^\circ$ would cause it to appear as it does. This viewing angle would imply a true expansion velocity of 97 km s⁻¹ which corresponds to an age of 70 kyr. However, if the remnant is indeed encountering denser material, it may have undergone a more abrupt (non-adiabatic) deceleration, and again, this expansion velocity is outside the expected range of the Sedov-Taylor phase, netting a younger age for a given observed radius and expansion velocity.

The uncertainty in the properties of this SNR makes it difficult to choose accurate parameters for the simulations. Moreover, our simulations are spherically symmetric, which is clearly not the case for this remnant. Simulations run over a range of reasonable parameters all result in fits with ages < 50 kyr, lending support to the above consideration.

5. Conclusions

We have presented a multi-wavelength study of three recently discovered SNRs in the LMC, featuring new *XMM-Newton* observations. We fit background spectra from each observation with a detailed model including soft proton contamination, instrumental lines, the local hot bubble, and extragalactic components. These fits gave consistent values for the background parameters across the three observations. We then fit source spectra with thermal plasma models, and compare the fits to simulated spectra. We analytically estimated the physical properties of the SNRs.

SNR0449–6921 is confirmed as an SNR due to its [SII]/Ha ratio, velocity expansion pattern, and soft X-ray emission, although we cannot fully characterise that emission. SNR0506–6542 appears from our findings to be a large, relatively old SNR, similar to SNR 0450–709. It has fairly disorganized expansion and X-ray emission that appears to be due to a combination of recently shocked material and older “fossil” radiation. SNR0537–6628 appears to be encountering higher density material to one side and shows signs of a bipolar expansion geometry. Although we were able to obtain good fits to its spectrum, the age is difficult to determine precisely due to uncertainties in its geometry and environment.

The authors would like to acknowledge David Henley for helpful comments and assistance in the conversion of the simulated spectra to Xspec models.

Cerro Tololo Inter-American Observatory (CTIO) is operated by the Association of Universities for Research in Astronomy Inc. (AURA), under a cooperative agreement with the National Science Foundation (NSF) as part of the National Optical Astronomy Observatories (NOAO). We gratefully acknowledge the support of CTIO and all the assistance which has been provided in upgrading the Curtis Schmidt telescope. The MCELS is funded through the support of the Dean B. McLaughlin fund at the University of Michigan and through NSF grant 9540747.

REFERENCES

Arabadjis, J. S., & Bregman, J. N. 1999, *ApJ*, 510, 806

- Blair, W. P., Ghavamian, P., Sankrit, R., & Danforth, C. W. 2006, *ApJS*, 165, 480
- Chen, L.-W., Fabian, A. C., & Gendreau, K. C. 1997, *MNRAS*, 285, 449
- Chu, Y.-H. 1997, *AJ*, 113, 1815
- Chu, Y.-H., & Mac Low, M.-M. 1990, *ApJ*, 365, 510
- Chu, Y.-H., Kim, S., Points, S. D., Petre, R., & Snowden, S. L. 2000, *AJ*, 119, 2242
- Chu, Y.-H., Weis, K., & Garnett, D. R. 1999, *AJ*, 117, 1433
- Di Benedetto, G. P. 2008, *MNRAS*, 390, 1762
- Dunne, B. C., Points, S. D., & Chu, Y.-H. 2001, *ApJS*, 136, 119
- Feast, M. 1999, *PASP*, 111, 775
- Fesen, R. A., Blair, W. P., & Kirshner, R. P. 1985, *ApJ*, 292, 29
- Filipovic, M. D., Haynes, R. F., White, G. L., & Jones, P. A. 1998, *Astron. Astrophys., Suppl. Ser.*, 130, 421
- Garnett, D. R., & Chu, Y.-H. 1994, *PASP*, 106, 626
- Haberl, F., & Pietsch, W. 1999, *Astron. Astrophys., Suppl. Ser.*, 139, 227
- Henley, D. B., & Shelton, R. L. 2008, *ApJ*, 676, 335
- Kalberla, P. W. M., Burton, W. B., Hartmann, D., Arnal, E. M., Bajaja, E., Morras, R., & Pöppel, W. G. L. 1999, *A&A*, 440, 775
- Kim, S., Staveley-Smith, L., Dopita, M. A., Sault, R. J., Freeman, K. C., Lee, Y., & Chu, Y.-H. 2003, *ApJS*, 148, 473
- Levenson, N. A., Kirschner, R. P., Blair, W. P., Winkler, P. F. 1995, *AJ*, 110, 739
- Pakull, M. W., & Angebault, L. P. 1986, *Nature*, 322, 511
- Pakull, M. W., & Motch, C. 1989, *Nature*, 337, 337
- Shelton, R. L. 1998, *ApJ*, 504, 785
- Smith, C., Leiton, R., & Pizarro, S. 2000, in *ASP Conf. Ser. 221, Stars, Gas and Dust in Galaxies: Exploring the Links*, ed. D. Alloin, K. Olsen, & G. Galaz (San Francisco, CA: ASP), 83
- Smith, R. C., Points, S., Chu, Y.-H., Winkler, P. F. 2003, *American Astronomical Society Meeting*, 203, 39.15
- Smith, R. C. et al. 2011, in preparation
- Snowden, S. L., Mushotzky, R. F., Kuntz, K. D., & Davis, D. S. 2008, *A&A*, 478, 615
- Stupar, M., Parker, Q. A., & Filipović, M. D. 2007, *AAONew*, 112, 12
- Turner, M. L. J., et al. 2001, *A&A*, 365, L27
- Williams, R. M., Chu, Y.-H., Dickel, J. R., Gruendl, R. A., Shelton, R., Points, S. D., Smith, & R. C. 2004, *ApJ*, 613, 948
- Williams, R. M., Chu, Y.-H., Dickel, J. R., Petre, R., Smith, R. C., & Tavaréz, M. 1999, *ApJS*, 123, 467

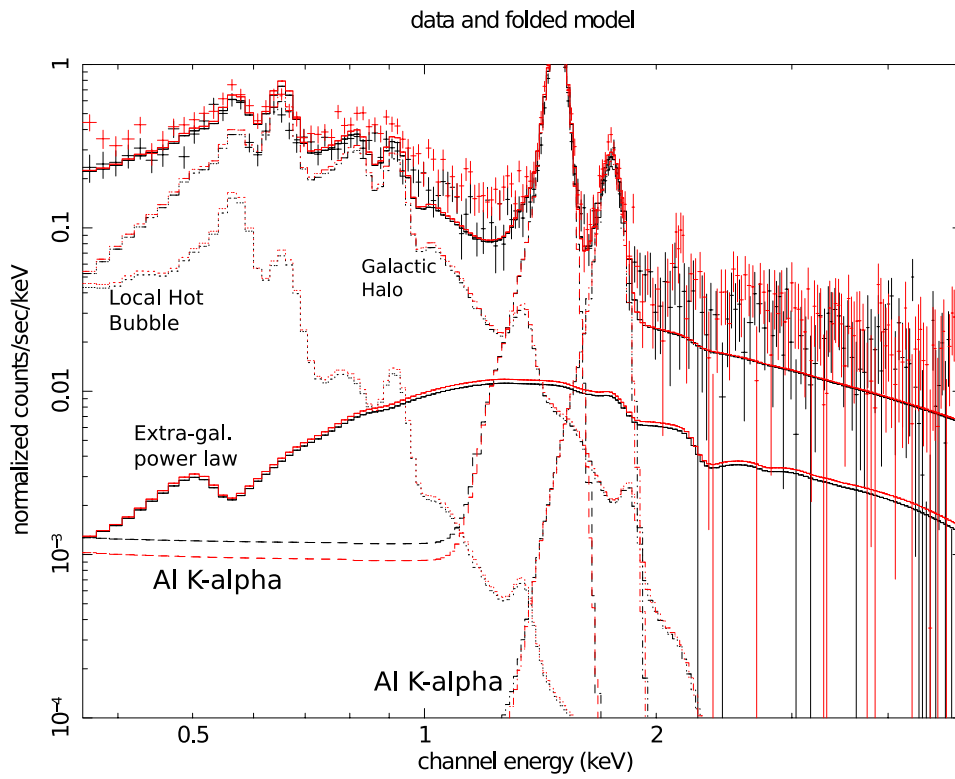


Fig. 1.— The background spectrum for SNR0506–6542 with individual components plotted and labeled.

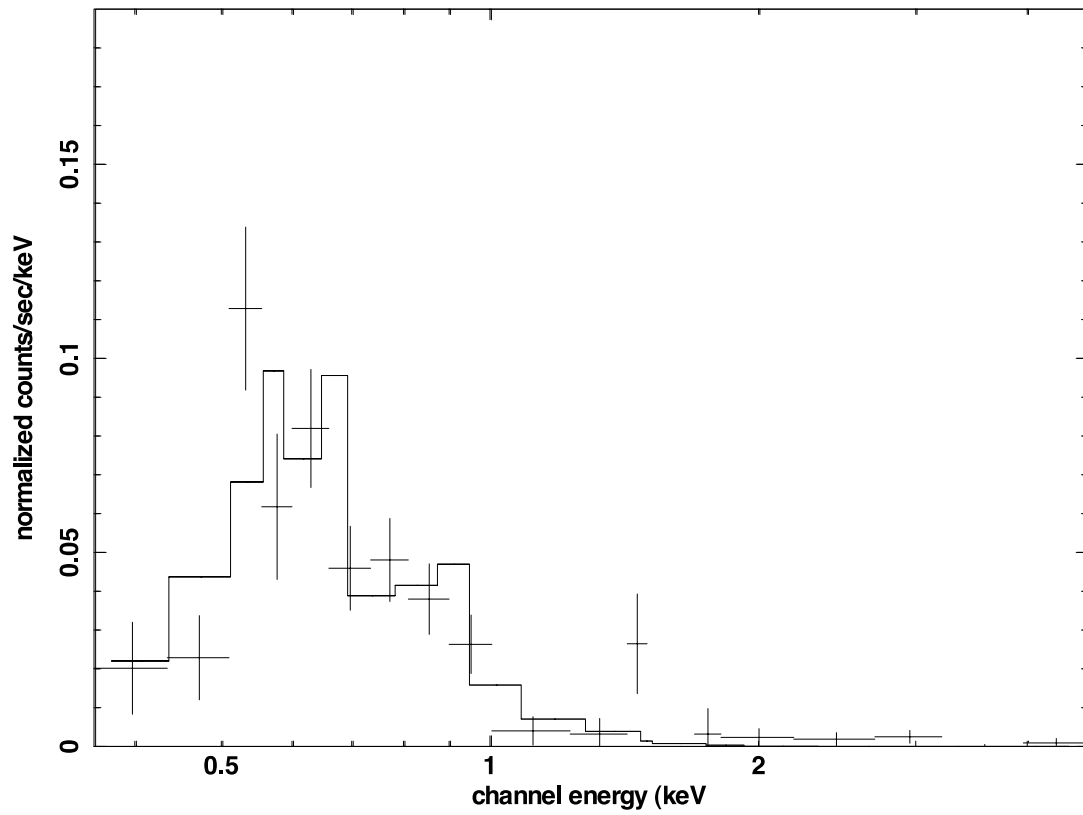


Fig. 2.— Background-subtracted source spectrum for SNR0506-6542 fitted with our source model.

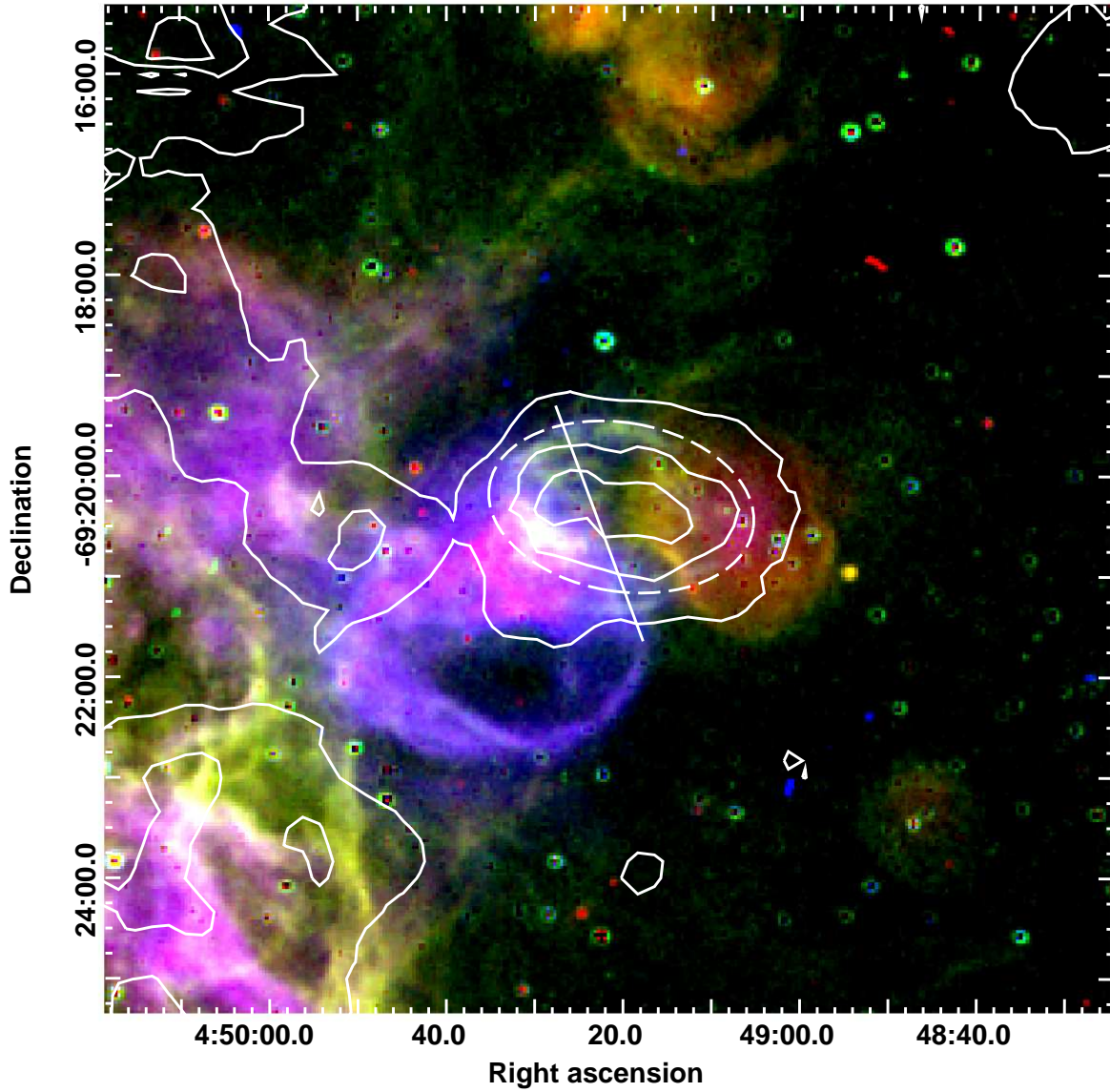


Fig. 3.— Three-color image of SNR0449–6921 with X-ray contours overlaid. Red is $H\alpha$, green is $[SII]$, and blue is $[OIII]$. Contours are at levels of 2 counts per second per square degree in the energy band 0.35–0.85 keV. The dashed ellipse corresponds to the SNR extent considered in the calculations of the X-ray and optical shell properties. The line corresponds to the radial slice shown in Figure 4.

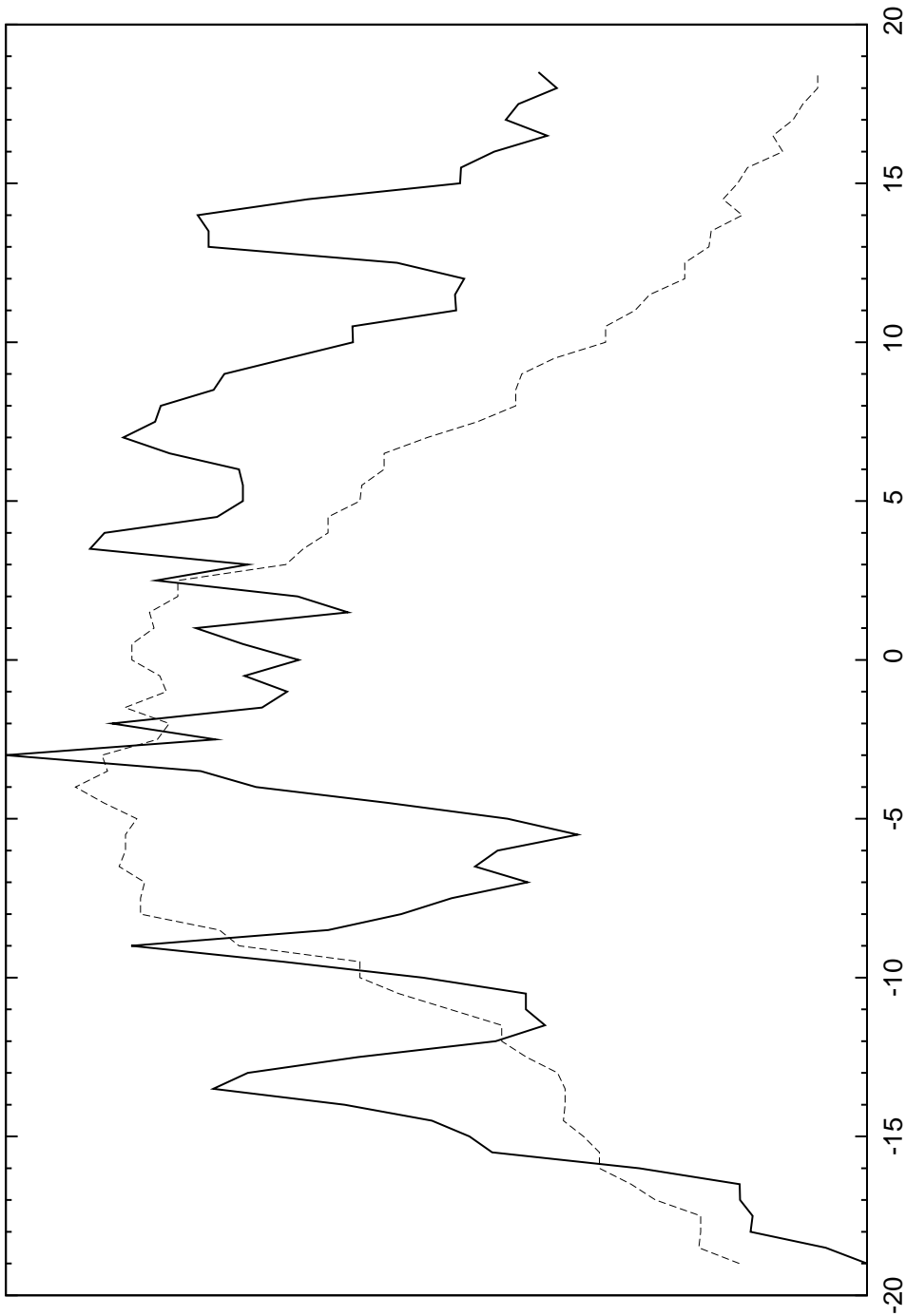


Fig. 4.— Radial profile of SNR0449–6921. The solid line represents H α and the dashed line represents 0.35–0.85 keV smoothed X-rays. X-axis units are parsecs. The origin corresponds to 04 49 22.74, -69 20 27.28. The slice was chosen so as to avoid the diffuse emission from the nearby H II region.

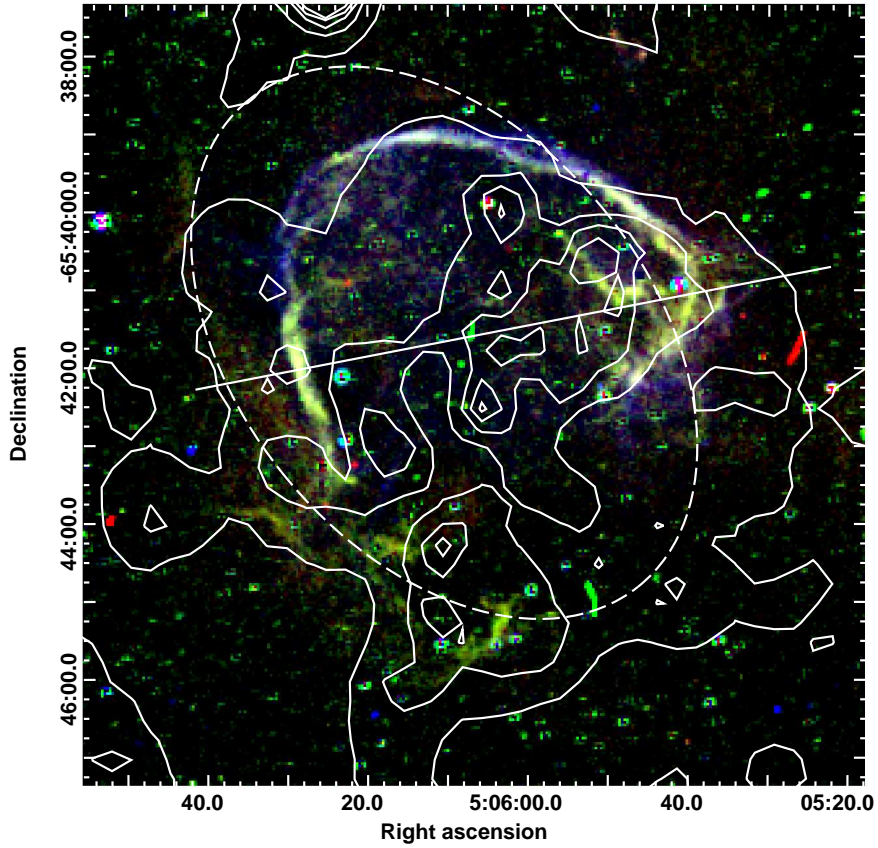


Fig. 5.— Three-color image of SNR0506–6542 with X-ray contours overlaid. Red is $H\alpha$, green is $[SII]$, and blue is $[OIII]$. Contours are at levels of 2 counts per second per square degree in the energy band 0.35–0.85 keV. The dashed ellipse corresponds to the SNR extent considered in the calculations of the X-ray and optical shell properties. The line corresponds to the radial slice shown in Figure 6.

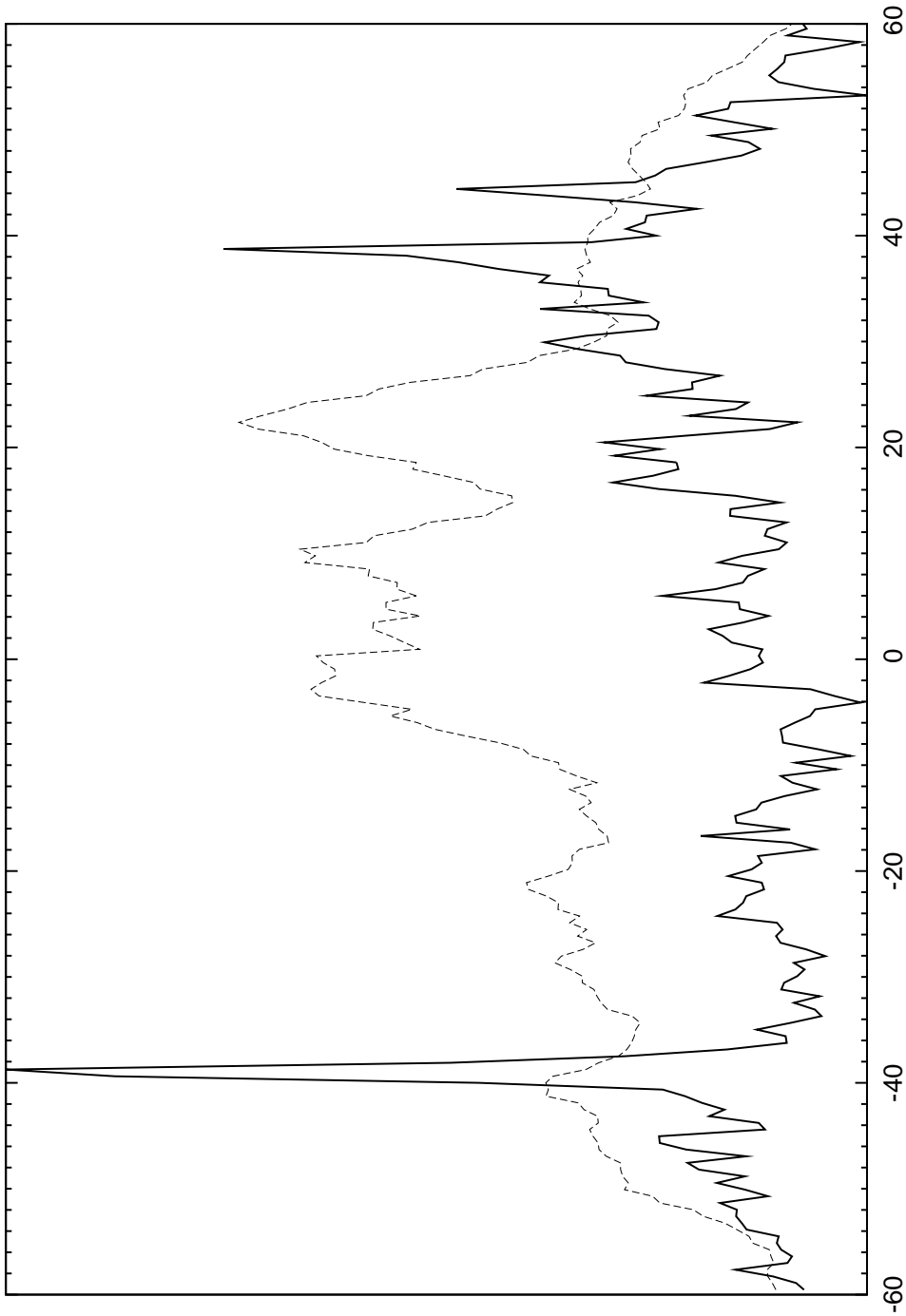


Fig. 6.— Radial profile of SNR0506–6542. The solid line represents H α and the dashed line represents 0.35–0.85 keV smoothed X-rays. X-axis units are parsecs. The origin corresponds to 05 06 01.87, -65 41 29.43. The northeastern spur is visible near -45.

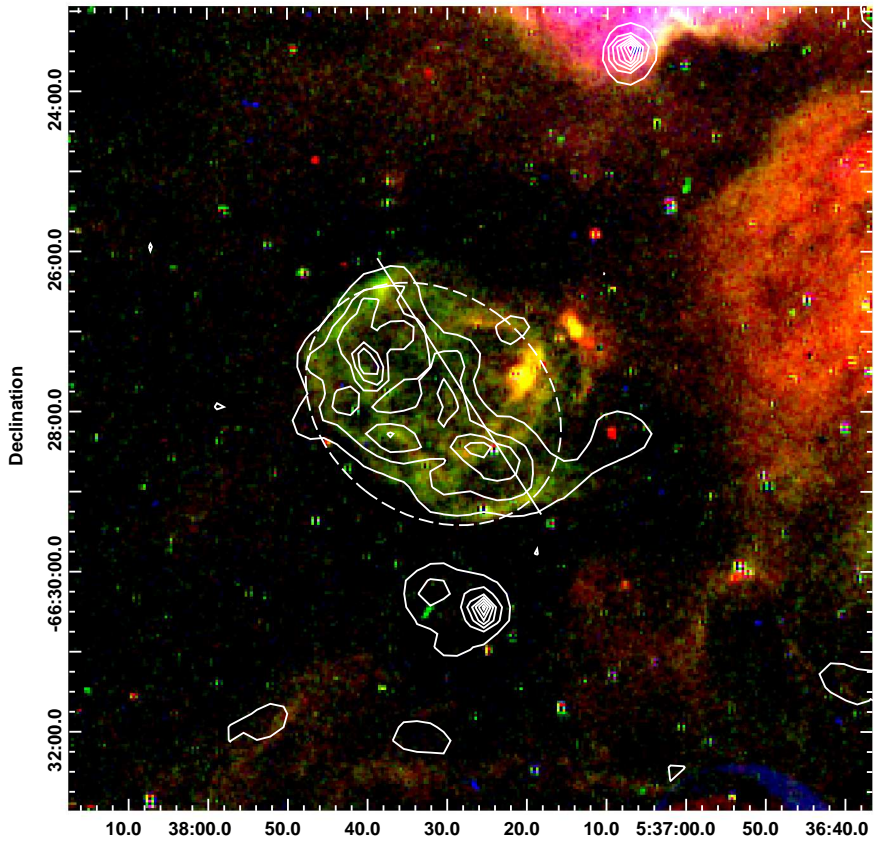


Fig. 7.— Three-color image of SNR0537-6628 with X-ray contours overlaid. Red is $H\alpha$, green is $[SII]$, and blue is $[OIII]$. Contours are at levels of 2 counts per second per square degree in the energy band 0.35–0.85 keV. The dashed ellipse corresponds to the SNR extent considered in the calculations of the X-ray and optical shell properties. The line corresponds to the radial slice shown in Figure 8.

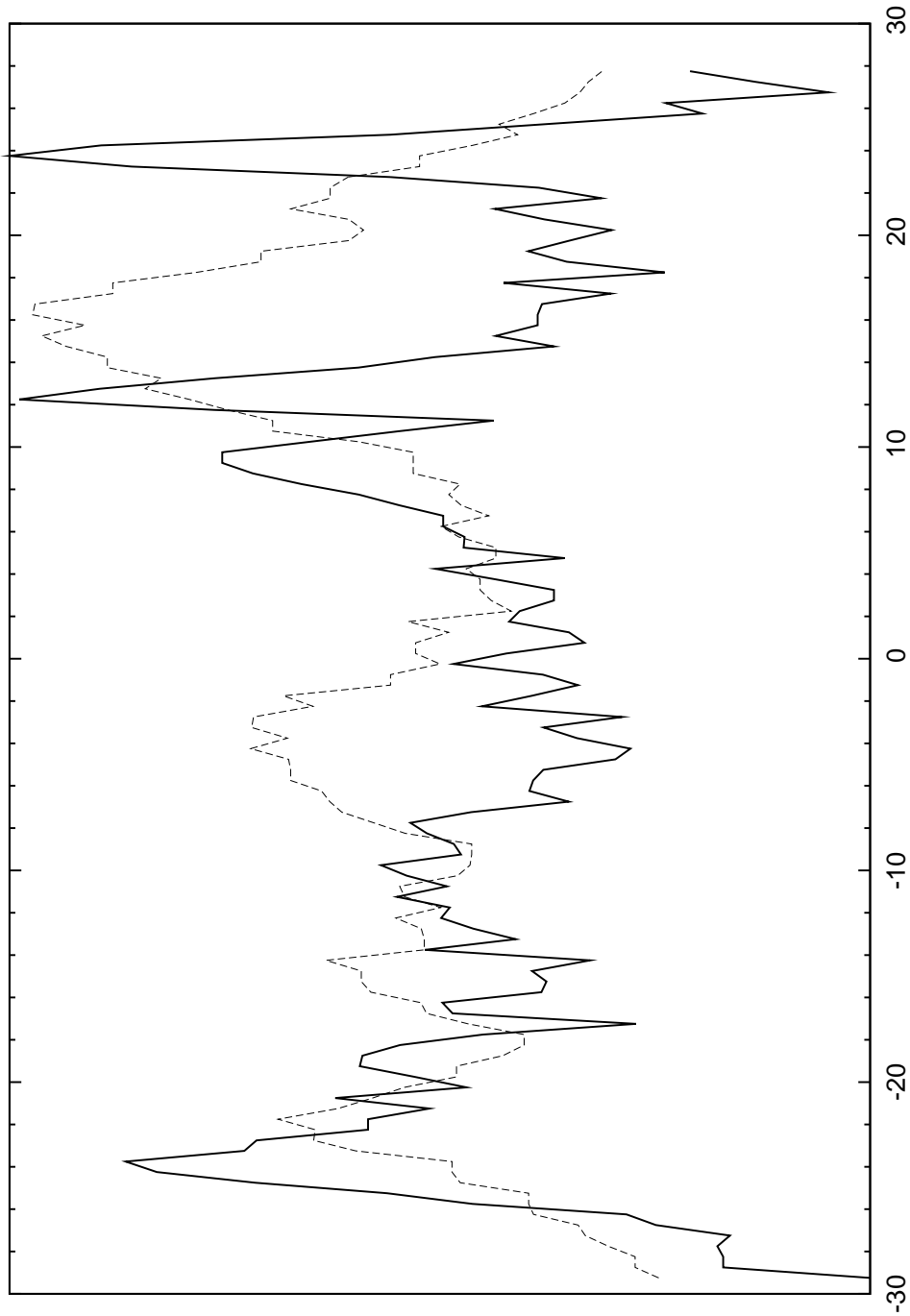


Fig. 8.— Radial profile of SNR0537–6628. The solid line represents $H\alpha$ and the dashed line represents 0.35–0.85 keV smoothed X-rays. X-axis units are parsecs. The origin corresponds to 05 37 28.49, -66 27 41.47. The slice was chosen to lie along the western extent of the outer shell.

TABLE 1
XMM-Newton OBSERVATION LOG

Obs ID	RA	Dec.	Start Time	Exp. Time (ks)
205260101	04h49m40.00s	-69°21'49.0"	2004-02-24 16:19:07	18.7
205260201	05h06m05.00s	-65°41'30.0"	2004-01-16 18:06:28	16.9
301410601	05h37m32.00s	-66°28'26.6"	2005-10-02 09:33:11	21.8

TABLE 2

PHYSICAL PROPERTIES OF SNRS. THE X-RAY FIT PARAMETERS ARE FROM AN APEC MODEL.

	SNR0449–6921	SNR0506–6542	SNR0537–6628
R (pc)	19×11	60×40	24×20
SB (10^{-15})	0.9	0.5	0.4
v_{exp} (km s $^{-1}$)	70	90	55
$n_{\text{e,shell}}$ (cm $^{-3}$)	5.5(2)	2.99(8)	3.30(4)
V_{shell} (cm 3)	1.4×10^{59}	1.7×10^{60}	3.2×10^{59}
M_{shell} (M_{\odot})	820(30)	$5.6(1) \times 10^3$	$1.14(1) \times 10^3$
K (erg)	$4(1) \times 10^{49}$	$4(1) \times 10^{50}$	$3(1) \times 10^{49}$
P_{shell} (dyne cm $^{-2}$)	$1.51(5) \times 10^{-11}$	$8.2(2) \times 10^{-12}$	$9.1(1) \times 10^{-12}$
kT (keV)		0.17(1)	0.22(5)
Normalization (10^{-14} cm $^{-5}$)		0.004(2)	0.0009(9)
V (cm 3)		$1.3(3) \times 10^{61}$	$1.0(1) \times 10^{60}$
$n_{\text{e,hot}}$ (cm $^{-3}$)		0.11(4)	0.2(2)
M_{hot} (M_{\odot})		$1.3(9) \times 10^3$	$2(2) \times 10^2$
E_{th} (erg)		$1.1(8) \times 10^{51}$	$2(2) \times 10^{50}$
P_{hot} (dyne cm $^{-2}$)		$5(2) \times 10^{-11}$	$1(1) \times 10^{-10}$
n_{ISM} (cm $^{-3}$)	> 4.0	0.5 1(1)	1.40(2)

TABLE 3
BACKGROUND SPECTRAL PARAMETERS

	SNR0449–6921 H II region	SNR0449–6921 clear region	SNR0506–6542	SNR0537–6628
Soft Proton Index	1.9(6)	1.9(6)	1.0(1)	1.39(7)
Soft Proton Norm. (cts keV ⁻¹ cm ⁻² s ⁻¹)	0.02(2)	0.003(3)	0.04(1)	0.048(5)
Local Bubble Temp. (keV)	0.11(1)	0.11(1)	0.09(1)	0.17(4)
Local Bubble Norm. (10 ⁻¹⁴ cm ⁻⁵)	4(4)×10 ⁻⁴	7(7)×10 ⁻⁴	0.002(2)	3(1)×10 ⁻⁴
N_{H} (10 ²² cm ⁻²)	0.37(7)	0.37(7)	0.32(7)	0.5(1)
Extragal. Thermal Temp. (keV)	0.27(4) 0.19(4)	0.27(4)	0.20(2)	0.22(2)
Extragal. Thermal Norm. (10 ⁻¹⁴ cm ⁻⁵)	7(7)×10 ⁻⁴ 0.02(1)	0.001(1)	0.003(2)	0.005(3)
Extragal. Norm. (10 ⁻⁴ cts keV ⁻¹ cm ⁻² s ⁻¹)	2(2)	2.1(7)	3(2)	0.9(9)